


Microscopic study on asymmetric fission dynamics of ^{180}Hg within covariant density functional theory

Zeyu Li ¹, Shengyuan Chen,¹ Yongjing Chen,^{2,*} and Zhipan Li ^{1,†}

¹*School of Physical Science and Technology, Southwest University, Chongqing 400715, China*

²*China Nuclear Data Center, China Institute of Atomic Energy, Beijing 102413, China*



(Received 18 April 2022; accepted 20 July 2022; published 4 August 2022)

The asymmetric fission dynamics of ^{180}Hg has been analyzed in the framework of the time-dependent generator coordinate method (TDGCM) based on covariant density functional theory (CDFT) with the relativistic PC-PK1 functional. Three-dimensional (β_2, β_3, q_N) constrained CDFT calculations have been performed to determine the scission configurations. Remarkably, an asymmetric fission valley is observed in the potential energy surface in the β_2 - β_3 plane and the heavy/light fragments at scission are $^{101}\text{Rh}/^{79}\text{Br}$, in good agreement with the data. Furthermore, we find that the heavy fragments of lowest-energy scission configurations, compared to those of other scission points, have rather small quadrupole deformations ($\beta_2 \sim 0.4$) and certain octupole deformations ($\beta_3 \sim 0.3$ – 0.4), which are driven by the extended neutron octupole shell gap with $N = 56$. Based on the scission configurations, the estimated total kinetic energy distribution is consistent with the trend of experimental data. Finally, the dynamical TDGCM calculation reproduces the asymmetric yield distribution of the low-energy fission of ^{180}Hg , especially for the peak positions.

DOI: [10.1103/PhysRevC.106.024307](https://doi.org/10.1103/PhysRevC.106.024307)

I. INTRODUCTION

The experimental discovery of asymmetric fission in ^{180}Hg via the β decay of ^{180}Tl initially came as a surprise since a mass-symmetric split of this extremely neutron-deficient nucleus was expected and would lead to two ^{90}Zr fragments, with magic $N = 50$ and semimagic $Z = 40$ [1–3]. This is regarded as a new type of asymmetric fission, not caused by large shell effects related to fragment magic proton and neutron numbers, as observed in the actinide region [4–7]. Since then, fission in the neutron-deficient lead region has attracted tremendous attention on both the experimental side [8–14] and theoretical side [15–29] in the last decade. Experimentally, the following measurements of fission fragment distribution from the compound nuclei around ^{180}Hg formed in fusion reactions have further confirmed the asymmetric property even for effective excitation energies up to 40 MeV [8–10].

Theoretically, the asymmetric fission of nuclei around ^{180}Hg has been extensively studied by analyzing the multidimensional potential energy surfaces (PESs) calculated from the macroscopic-microscopic models and it is explained as the presence of an asymmetric saddle point with a rather high ridge between symmetric and asymmetric fission valleys [1, 15–20]. Calculations of fission-fragment yields have also been done by means of the Brownian Metropolis shape-motion treatment [15–17], Langevin equation [21], (improved) scission-point model [22–24], etc., based on the PESs or scission configurations. The results are in approxi-

mate agreement with the experimental data, a deviation of ~ 4 nucleons for the peak positions.

A comprehensive explanation of nuclear fission based on realistic nucleon-nucleon interaction still eludes us, and therefore, self-consistent approaches based on the nuclear density functional theory (DFT) have recently demonstrated that a microscopic description has a potential for both qualitative and quantitative description of fission data [30–35]. The Skyrme and Gogny energy density functionals have been used to investigate the asymmetric fission around ^{180}Hg based on the potential energy surfaces in the multidimensional space of collective coordinates. The asymmetric fission valleys—well separated from fusion valleys associated with nearly spherical fragments—are found and the most probable split $^{100}\text{Ru}/^{80}\text{Kr}$ is obtained by analyzing the density distributions at scission configurations, which is consistent with the observation [26, 29]. Furthermore, the study is extended to the case with excitation energy up to 30 MeV by using finite-temperature DFT and demonstrates that fission pathways are consistent with asymmetric fission at low excitation energies, with the symmetric-fission pathway opening very gradually as excitation energy increases [27]. Moreover, the asymmetric fission in the sub-lead region is explained as the shell effects stabilizing pear shapes of the fission fragments based on the static Hartree-Fock+BCS calculations [28]. However, the dynamical calculation based on DFT is lacking until now.

Microscopic description of fission dynamics based on DFT is generally implemented in two ways, i.e., time-dependent DFT (TDDFT) [32, 36–43] and the time-dependent generator coordinate method (TDGCM) [30, 34, 44–56]. The fully microscopic and nonadiabatic TDDFT describes the dynamics of the fission process starting from an adiabatic configuration just beyond the saddle and ending with separate fragments. It

*ahchenyj@126.com

†zpliphy@swu.edu.cn

has been shown that many collective degrees of freedom are excited in the fission process, and that one-body dissipation plays an important role [57]. Physical observables such as the most probable charge, mass, and total kinetic energy yields can be extracted from the TDDFT calculations. However, a realistic TDDFT description of the entire fission process, including the first phase from the ground-state potential well to beyond the fission barrier, is still not possible although some attempts have been done recently [58,59]. This prevents the application of TDDFT to the sub-lead region, where the nucleus splits just after saddle as shown in the DFT calculations [26,27].

In the TDGCM approach, the nuclear wave function is described as a linear superposition of many-body functions parametrized by a vector of collective coordinates, e.g., quadrupole and octupole deformations β_2, β_3 . In the Gaussian overlap approximation (GOA), the GCM Hill-Wheeler equation reduces to a local, time-dependent, Schrödinger-like equation in the space of collective coordinates. Starting from an initial state of the compound nucleus, the adiabatic time evolution of the fissioning system is modeled with the Schrödinger-like equation and the fission fragment distribution can be obtained by considering the flux of the probability current through the scission hypersurface. The essential inputs are the potential and inertia tensor that can be computed microscopically in DFT calculation. The TDGCM+GOA based on nonrelativistic Skyrme or Gogny functionals has been applied to describe fission dynamics of actinides in several studies [34,44–50]. In Refs. [51–56], the framework has also been successfully implemented based on the (finite-temperature) covariant DFT (CDFT) and applied to the description of induced fission in a series of nuclei in the actinide region. The fission fragment yields can be reproduced quite well.

In this work, we will apply the TDGCM+GOA based on CDFT to describe the asymmetric fission dynamics of ^{180}Hg . Considering the importance of scission configurations in the TDGCM+GOA calculation, here we will extend our previous two-dimensional (β_2, β_3) constraint calculations around scission to three dimensions by adding q_N , the number of nucleons in the neck, and define the saddle between fission and fusion valleys as the scission point. This can solve the problem of discontinuity of the configurations around the scission point in the two-dimensional calculations [60]. Moreover, we will analyze the PESs and single-particle levels of fragments to try to understand the formation of the asymmetric fission valley. The theoretical framework and methods are introduced briefly in Sec. II. The details of the calculation and the results for potential energy surfaces, scission configurations, total kinetic energies, and the fragment mass yield distributions are described and discussed in Sec. III. Section IV contains a summary of the principal results and an outlook for future work.

II. THEORETICAL FRAMEWORK

Nuclear fission is a slow and large-amplitude collective motion, and can be described as a collective wave function with some collective degrees of freedom, e.g., axially

symmetric quadrupole β_2 and octupole β_3 being used here. The low-energy fission dynamics could be simulated by a time-dependent Schrödinger-like equation which is derived from the TDGCM in the Gaussian overlap approximation (GOA) [30,34,45]:

$$i\hbar \frac{\partial}{\partial t} g(\beta_2, \beta_3, t) = \left[-\frac{\hbar^2}{2} \sum_{kl} \frac{\partial}{\partial \beta_k} B_{kl}^{-1}(\beta_2, \beta_3) \frac{\partial}{\partial \beta_l} + V(\beta_2, \beta_3) \right] \times g(\beta_2, \beta_3, t), \quad (1)$$

where $g(\beta_2, \beta_3, t)$ is a complex wave function of the collective variables (β_2, β_3) and time t , which contains all the information about the dynamics of the system. $V(\beta_2, \beta_3)$ and $B_{kl}(\beta_2, \beta_3)$ are the collective potential and mass tensor, respectively, and they completely determine the dynamics of the fission process in the TDGCM+GOA framework. Following our previous work [51], the software package FELIX-2.0 [61] is utilized to solve the time-dependent Schrödinger-like equation.

Then we can calculate the probability current defined by the relation

$$J_k(\beta_2, \beta_3, t) = \frac{\hbar}{2i} \sum_{l=2}^3 B_{kl}^{-1}(\beta_2, \beta_3) \left[g^*(\beta_2, \beta_3, t) \frac{\partial g(\beta_2, \beta_3, t)}{\partial \beta_l} - g(\beta_2, \beta_3, t) \frac{\partial g^*(\beta_2, \beta_3, t)}{\partial \beta_l} \right]. \quad (2)$$

Starting from an initial state of the compound nucleus, the collective current will move to a large deformation region and pass through a so-called scission line that is composed of the hypersurface at which the nucleus splits. At the time t , the measurement of the probability of a given pair of fragments can be calculated when the flux of the probability current runs through the scission hypersurface. For a surface element ξ , the sum of the time-integrated flux of the probability $F(\xi, t)$ can be read as [61]

$$F(\xi, t) = \int_{t=0}^t dt \int_{(\beta_2, \beta_3) \in \xi} \mathbf{J}(\beta_2, \beta_3, t) \cdot d\mathbf{S}. \quad (3)$$

For each point on the scission line, it contains the information of (A_L, A_H) which represent the masses of light and heavy fragments, respectively. Hence the yield of fission fragments with mass A_H can be defined formally as

$$Y(A_H) \propto \sum_{\xi \in \mathcal{A}} \lim_{t \rightarrow +\infty} F(\xi, t), \quad (4)$$

where \mathcal{A} is the set of all elements ξ belonging to the scission hypersurface such that the heavy fragment has mass A_H .

The entire dynamics of the Schrödinger-like equation (1) is governed by the collective potential V and mass parameter B , which are determined by performing constrained CDFT calculations for a specific choice of the nuclear energy density functional and pairing interaction. The entire map of the energy surface in collective space is obtained by imposing constraints on the collective coordinates. As mentioned above, the scission configurations in the TDGCM+GOA calculation

are very important. Therefore, here we will extend our previous two-dimensional (β_2, β_3) constraint calculations around scission to three dimensions by adding q_N , the number of nucleons in the neck:

$$\langle E_{\text{CDFT}} \rangle + \sum_{k=2,3} C_k (\langle \hat{Q}_k \rangle - q_k)^2 + C_N (\langle \hat{Q}_N \rangle - q_N)^2, \quad (5)$$

where $\langle E_{\text{CDFT}} \rangle$ is the total energy of CDFT, and \hat{Q}_2 , \hat{Q}_3 , and \hat{Q}_N denote the mass quadrupole and octupole operators and the Gaussian neck operator, respectively. q_k and q_N are the constraint values of these operators. The Gaussian neck operator is generally chosen as $\hat{Q}_N = \exp[-(z - z_N)^2/a_N^2]$, where $a_N = 1$ fm and z_N is the position of the neck determined by minimizing $\langle \hat{Q}_N \rangle$ [62]. The left and right fragments are defined as parts of the whole nucleus with $z \leq z_N$ and $z \geq z_N$, respectively. One should note that the three-dimensional (3D) constrained calculation is only performed to determine the scission configuration and fission path around it. The fully 3D dynamical calculation is our next step. The microscopic computation for the collective potential V and mass parameter B can be found in Ref. [51].

III. RESULTS AND DISCUSSION

In this section, we present the theoretical results for the asymmetric fission of ^{180}Hg . In the first step, a large-scale constrained CDFT calculation with the PC-PK1 functional [63] is performed to generate the potential energy surface, mass parameters, scission line, and so on. The range of collective variables is -1.00 to 4.70 for β_2 with a step $\Delta\beta_2 = 0.04$, from 0.00 to 3.84 for β_3 with a step $\Delta\beta_3 = 0.08$, and from ~ 5 to ~ 1.5 with $\Delta q_N = 0.5$ (q_N constraint is done only around scission line). The self-consistent Dirac equation for the single-particle wave functions is solved by expanding the nucleon spinors in an axially deformed harmonic oscillator basis in cylindrical coordinates with 18 major shells, and the number of states in the Fermi sea for protons or neutrons reaches 1941 at $\beta_2 = 4.5$ as an example.

Figures 1(a) and 1(b) display the three-dimensional PES and corresponding two-dimensional contour map for ^{180}Hg in the β_2 - β_3 plane calculated by constrained CDFT with the PC-PK1 functional. The energy difference between neighboring contour lines is 1.2 MeV. The purple solid and red dotted curves denote the static fission path and scission line, respectively. The scission line is determined by checking the PESs in the β_2 - q_N plane for each β_3 , e.g., the PES for $\beta_3 = 2.08$ in the inset of panel (b). We can see clearly the fission valley and fusion valley, and they are separated by a saddle point (denoted by a filled circle), which is chosen as the scission point here.

The PES of ^{180}Hg in the quadrupole-octupole space is comparable to those obtained using the Hartree-Fock-Bogoliubov framework based on the Gogny D1S functional [26] and Skyrme SkM* functional [26,27]. The static fission path starts from a nearly spherical equilibrium state, passes through three local minima with $\beta_3 = 0$, and then bends toward reflection asymmetry at $\beta_2 = 0.98$ till scission at $(\beta_2, \beta_3) = (4.38, 2.08)$. This scission point is 12.17 MeV higher than the equilibrium state and the heavy/light fragments are

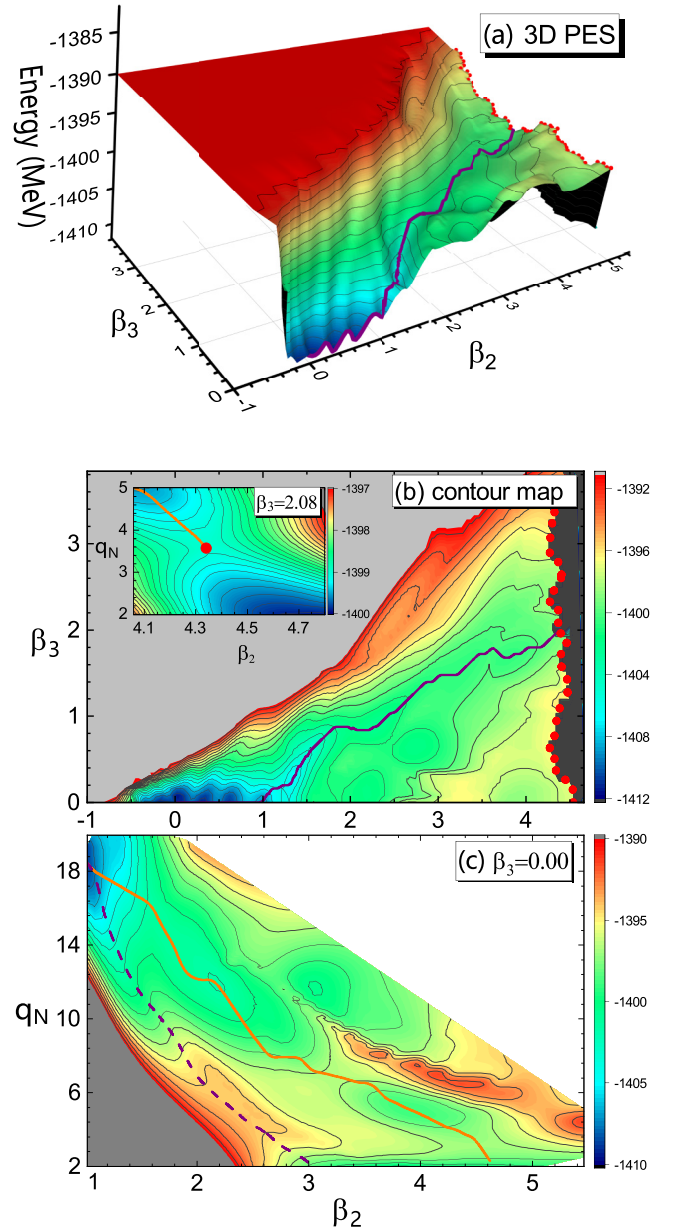


FIG. 1. Potential energy surfaces of ^{180}Hg in the β_2 - β_3 plane [panels (a), (b)] and in the β_2 - q_N plane for fixed $\beta_3 = 0.00$ [panel (c)] and $\beta_3 = 2.08$ [inset of panel (b)] calculated by the constrained CDFT with PC-PK1 functional. The purple solid and red dotted curves in panels (a), (b) denote the static fission path and scission line, respectively. The filled circle in the inset of panel (b) denotes the scission point. The symmetric elongated and compact fission modes are shown by the solid and dashed curves, respectively, in panel (c).

$^{101}\text{Rh}/^{79}\text{Br}$, in good agreement with the masses observed experimentally [1]. Moreover, another fission valley from $(\beta_2, \beta_3) \approx (2.60, 0.60)$ to $\approx (4.50, 0.00)$ is also found. However, the symmetric scission point, which splits into two ^{90}Zr , is 2.33 MeV higher than the asymmetric one. This will lead to an asymmetric yield distribution in the low-energy fission of ^{180}Hg (cf. Fig. 6).

In Fig. 1(c), a symmetric compact fission mode denoted by the dashed curve is also found, and the fragments are two nearly spherical ^{90}Zr with magic $N = 50$ and semimagic $Z = 40$. However, this mode is unfavored since the barrier is ~ 5 MeV higher than the lowest asymmetric scission point and ~ 2.5 MeV higher than the saddle point of the symmetric elongated fission path (orange solid curve). This is different from the case in the region around ^{264}Fm , where the symmetric compact fission mode splitting into two ^{132}Sn is dominated.

Figure 2 displays the properties of scission configurations, including the potential energies, mass and neutron numbers of heavy fragments, and quadrupole and octupole deformations of fragments. Nucleon density distributions for four selected configurations are also shown in panel (a), where one can see clearly the formation of necks and left/right fragments. As the reflection asymmetry increases, the potential energies vary slowly around -1397 MeV till $\beta_3 \sim 1.5$, then drop rapidly to ~ -1399 MeV at $\beta_3 \sim 2.0$, and finally increase monotonically to very large β_3 . From panels (b) and (c), one notes that the mass (neutron) numbers of heavy fragments for the scission points around minimum in panel (a) are $A_H = 96 \sim 106$ ($N_H = 54 \sim 58$), corresponding to the peak region of the yield distribution of fission fragments [1]. Furthermore, it is remarkable to find that these scission configurations are characterized by rather small quadrupole deformations of heavy fragments [see panel (d)], which are quite different from those in other regions. The octupole deformations of heavy fragments remain $0.3 \sim 0.4$ for the scission configurations with $\beta_3 < 2.8$ and jump to ~ 0.6 for large reflection asymmetric scission configurations.

To understand the dramatic change of the configurations around the minimum of the scission line, in Figs. 3 and 4 we plot the PES and neutron single-particle levels of ^{100}Ru , the most favorable even-even fragment in the fission of ^{180}Hg . In the PES plot, the star denotes the quadrupole and octupole deformations of the heavy fragment at the energy minimum of scission line. One should note that this is just an estimation for the deformations of the fragments since they are connected by a neck but not separated. It is interesting to find that the heavy fragment locates around a shallow valley from the global minimum $(\beta_2, \beta_3) = (0.2, 0)$ to $\approx (0.4, 0.5)$, which could lower the binding energy of the whole system. Furthermore, one finds that the shallow valley in the PES of ^{100}Ru is driven by the extended octupole shell gap with $N = 56$, shown in Fig. 4. This finding is consistent with that in a similar microscopic analysis of the effect of shell structure on the fission in the sub-lead region based on the Skyrme Hartree-Fock plus BCS approach. It is notable that the appearance of $N = 56$ as well as heavy fragment ^{100}Ru does not necessarily reduce the binding of scission configuration, e.g., those with $\beta_3 \sim 1.1$ in Fig. 2, where the potential energies are even 3 MeV higher than the minimum.

The Coulomb repulsive energy of fission fragments is the main component of the total kinetic energy (TKE) and can be estimated by using a simple formula $e^2 Z_H Z_L / d_{\text{ch}}$, where Z_H (Z_L) is the charge of the heavy (light) fragment and d_{ch} the distance between fragment centers of charge at scission. Figure 5 displays the distribution of calculated Coulomb repulsive energy and compared with the measured TKE [3].

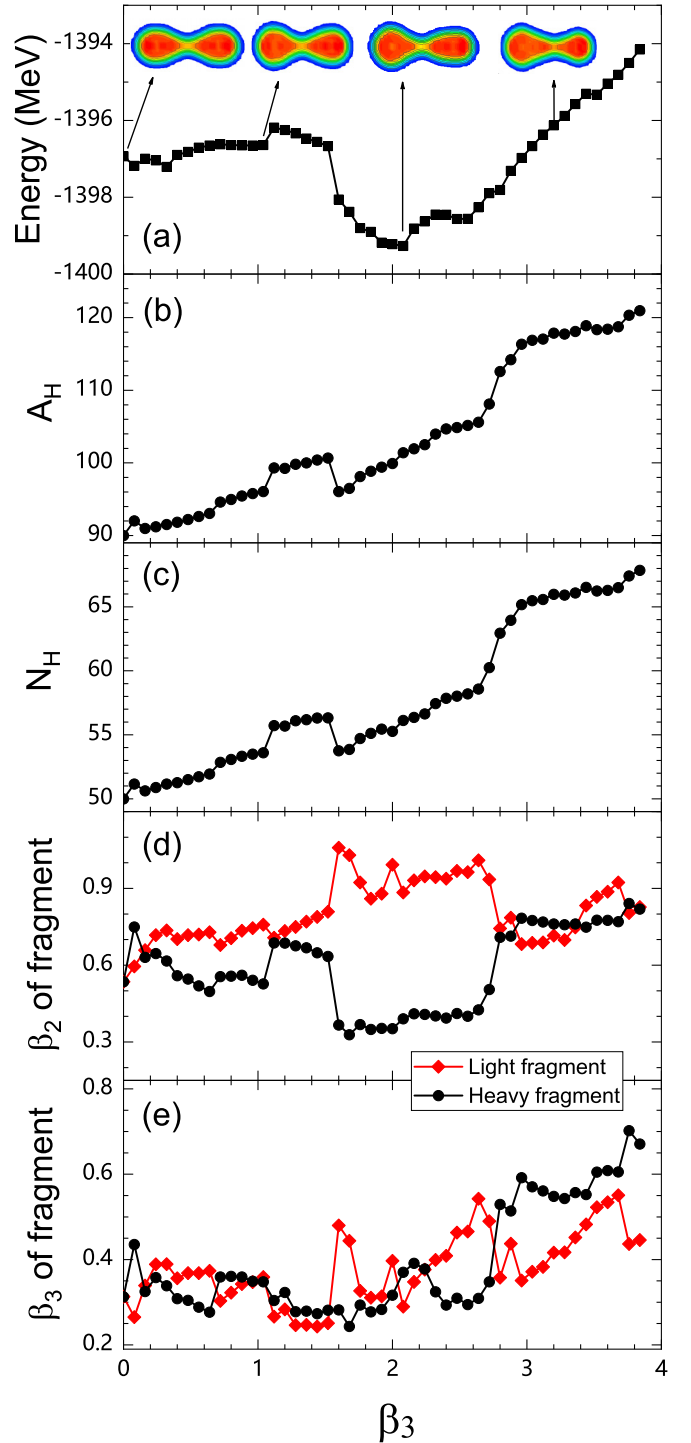


FIG. 2. The potential energies (a) and mass (b) and neutron (c) numbers of heavy fragments, and quadrupole (d) and octupole (e) deformations of fragments along the scission line labeled by the corresponding β_3 value. Density distributions for some selected scission configurations are also shown in panel (a).

Although the data are generally overestimated by about several MeV, the figure reproduces the trend of the measured TKE quite well, especially for the dip at $A_H = 90$ and peaks at $A_H = 94$ and 104. This demonstrates that the scission con-

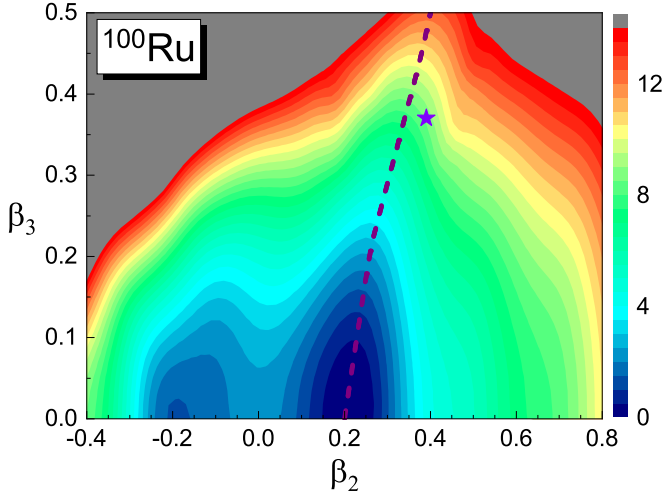


FIG. 3. Potential energy surfaces of ^{100}Ru calculated by CDFT with PC-PK1 functional. The star indicates the corresponding quadrupole and octupole deformations of the heavy fragment at the minimum of the scission point. The purple dashed curve denotes the configurations obtained by only constraining β_3 and leaving β_2 as free.

figurations determined in the three-dimensional calculations (cf. Fig. 1) are quite reliable, which is very important for the study of fission dynamics. To give a more accurate description of TKE, one needs to calculate the Coulomb energy between two fragments exactly based on the proton density distribution and take into account the collective kinetic energy. Such work is in progress.

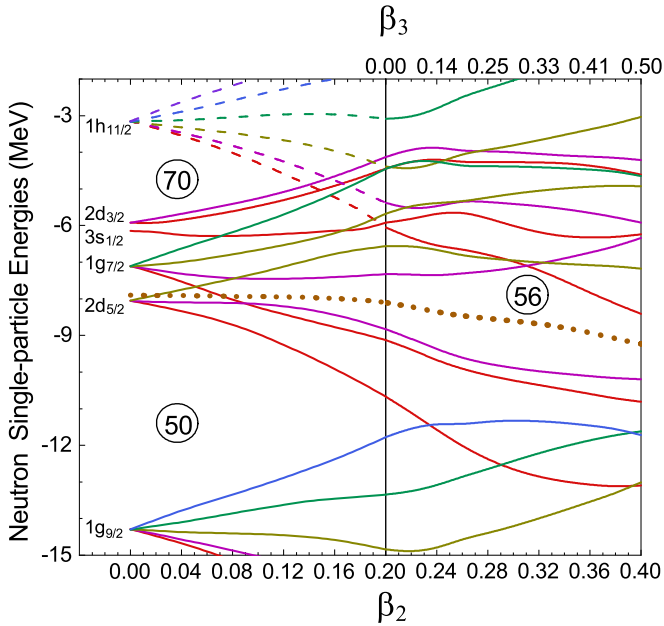


FIG. 4. Neutron single-particle energies as a function of the quadrupole (lower scale) and octupole (upper scale) deformation parameters in ^{100}Ru . The dotted curve denotes the Fermi level. The left panel is for $\beta_3 = 0$, and the right panel is plotted following the purple dashed curve in Fig. 3.

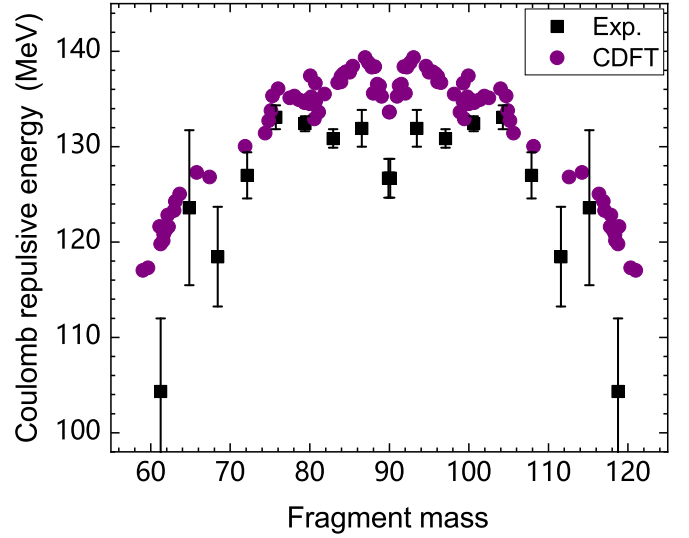


FIG. 5. The calculated Coulomb repulsive energy of the nascent fission fragments for ^{180}Hg as a function of fragment mass, in comparison to the experimental data of the total kinetic energy [3].

Finally, we perform the TDGCM+GOA [61] to model the time evolution of the fissioning nucleus with a time step $\delta t = 5 \times 10^{-4}$ zs and a long enough evolution time, i.e., 1000 zs, to ensure the convergence of the yield distribution. The initial state, in principle, should be a series of final states from electron capture (EC) of ^{180}Tl , lying in the vicinity of the fission barrier in ^{180}Hg . Here, for simplicity, we follow Ref. [61] to simulate the initial state as a Gaussian superposition of collective eigenmodes in an extrapolated first potential well and the average energy lies 1 MeV above the lowest scission point [cf. Fig. 2(a)].

Figure 6 shows the calculated mass distribution of the fission fragments of ^{180}Hg , in comparison with the data [1,3] and the theoretical results in the framework of Brownian shape motion on five-dimensional potential energy surfaces, denoted as BSM(M) [15]. The asymmetric peaks are reproduced by TDGCM+GOA based on CDFT very well not only for the positions but also for the heights considering the error bar of the data, while the results of BSM(M) deviate from the measured peak position by ~ 4 . For the symmetric valley, our calculation overestimates the data and even predicts a little peak, which may be caused by the fission valley from $(\beta_2, \beta_3) \approx (2.60, 0.60)$ to $\approx (4.50, 0.00)$ in the potential energy surface (cf. Fig. 1). Moreover, a more asymmetric fission mode with $A_H \sim 116$ is predicted in our calculation, corresponding to the shallow channel from $(\beta_2, \beta_3) \approx (3.70, 2.00)$ to $\approx (4.10, 2.48)$ in Fig. 1(b). However, this peak is not observed in the experiment, which could be because we use an initial state with mixed angular momenta but the experimental ones only have some certain values due to the selection rule of EC.

IV. SUMMARY AND OUTLOOK

The asymmetric fission dynamics of ^{180}Hg has been analyzed in the framework of TDGCM+GOA based on CDFT

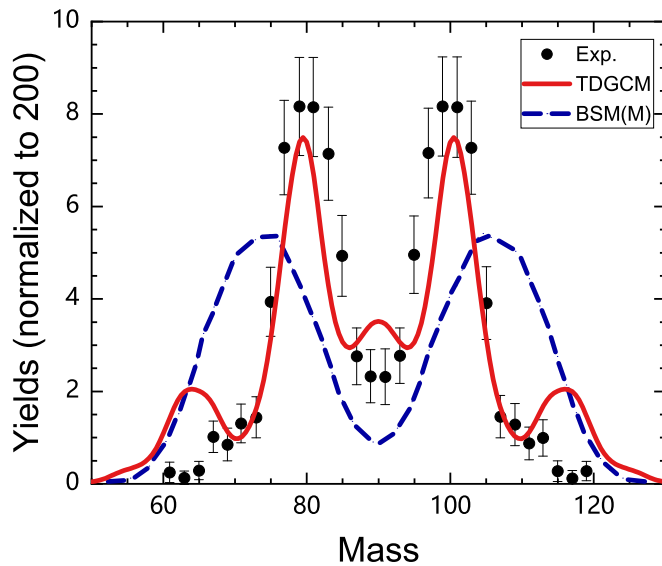


FIG. 6. Mass distribution of the fission fragments of ^{180}Hg calculated by TDGCM+GOA based on CDFT, in comparison with the data [1,3] and the theoretical results in the framework of Brownian shape motion on five-dimensional potential energy surfaces, denoted as BSM(M) [15].

with relativistic PC-PK1 functional. To provide more reliable scission configurations, three-dimensional (β_2, β_3, q_N) constrained CDFT calculations have been performed and the saddles between fission and fusion valleys have been defined as the scission points. It is remarkable to find an asymmetric fission valley in the potential energy surface in the quadrupole octupole collective space and the heavy/light fragments at scission are $^{101}\text{Rh}/^{79}\text{Br}$, in good agreement with the masses observed experimentally. In contrast, the symmetric scission point, which splits into two ^{90}Zr , is 2.33 MeV higher than the asymmetric one. Furthermore, we find that the heavy frag-

ments of lowest-energy scission configurations, compared to those of other scission points, have rather small quadrupole deformations ($\beta_2 \sim 0.4$) and certain octupole deformations ($\beta_3 \sim 0.3\text{--}0.4$), which are driven by the extended neutron octupole shell gap with $N = 56$. Based on the scission configurations, the estimated distribution of total kinetic energy reproduces the trend of experimental values. Finally, we have performed the TDGCM+GOA based on the microscopic PES and inertia masses to model the time evolution of the fissioning ^{180}Hg . The asymmetric peaks are reproduced very well not only for the positions but also for the heights considering the error bar of the data. Moreover, a more asymmetric fission mode with $A_H \sim 116$ is predicted in our calculation, which is not observed in the experiment. This could be because we use an initial state with mixed angular momenta but the experimental ones only have some certain values due to the selection rule of electron capture of ^{180}Tl .

The next step could be to construct the initial state based on the angular momentum projected states of ^{180}Hg , simulate the fission procedure for each possible state using TDGCM+GOA, and finally mix the products of all the simulations by considering the branching ratios of EC of ^{180}Tl . In addition, we could also extend our two-dimensional TDGCM+GOA calculation to include q_N to consider more fission modes based on a powerful CDFT code using a two-center harmonic oscillator basis. Such work is in progress. It is also interesting and necessary to perform a systematic calculation for the sub-lead region using the extended model to provide a better description of the yield distributions and underlying microscopic mechanism.

ACKNOWLEDGMENTS

This work was partly supported by the National Natural Science Foundation of China (Grants No. 11790325, No. 11875225, and No. 11790320), the Fundamental Research Funds for the Central Universities, and the Fok Ying-Tong Education Foundation.

- [1] A. N. Andreyev *et al.*, New Type of Asymmetric Fission in Proton-Rich Nuclei, *Phys. Rev. Lett.* **105**, 252502 (2010).
- [2] A. N. Andreyev, M. Huyse, and P. Van Duppen, Colloquium: Beta-delayed fission of atomic nuclei, *Rev. Mod. Phys.* **85**, 1541 (2013).
- [3] J. Elseviers *et al.*, β -delayed fission of ^{180}Tl , *Phys. Rev. C* **88**, 044321 (2013); **102**, 019908(E) (2020).
- [4] M. Brack, J. Damgaard, A. S. Jensen, H. C. Pauli, V. M. Strutinsky, and C. Y. Wong, Funny hills: The shell-correction approach to nuclear shell effects and its applications to the fission process, *Rev. Mod. Phys.* **44**, 320 (1972).
- [5] B. D. Wilkins, E. P. Steinberg, and R. R. Chasman, Scission-point model of nuclear fission based on deformed-shell effects, *Phys. Rev. C* **14**, 1832 (1976).
- [6] D. Gorodisskiy, S. Mulgin, V. Okolovich, A. Rusanov, and S. Zhdanov, Isotopic and isotonic effects in fission-fragment mass yields of actinide nuclei, *Phys. Lett. B* **548**, 45 (2002).
- [7] K.-H. Schmidt, A. Kelic, and M. Valentina Ricciardi, Experimental evidence for the separability of compound-nucleus and fragment properties in fission, *Europhys. Lett.* **83**, 32001 (2008).
- [8] K. Nishio *et al.*, Excitation energy dependence of fragment-mass distributions from fission of $^{180,190}\text{Hg}$ formed in fusion reactions of $^{36}\text{Ar} + ^{144,154}\text{Sm}$, *Phys. Lett. B* **748**, 89 (2015).
- [9] E. Prasad *et al.*, Observation of mass-asymmetric fission of mercury nuclei in heavy ion fusion, *Phys. Rev. C* **91**, 064605 (2015).
- [10] T. N. Nag, R. Tripathi, S. Patra, A. Mhatre, S. Santra, P. C. Rout, A. Kundu, D. Chattopadhyay, A. Pal, and P. K. Pujari, Fission fragment mass distribution in the $^{32}\text{S} + ^{144}\text{Sm}$ reaction, *Phys. Rev. C* **103**, 034612 (2021).
- [11] L. Ghys *et al.*, Evolution of fission-fragment mass distributions in the neutron-deficient lead region, *Phys. Rev. C* **90**, 041301(R) (2014).

- [12] D. Paul, A. Sen, T. K. Ghosh, M. Moin Shaikh, K. Atreya, S. Kundu, K. Banerjee, C. Bhattacharya, S. Bhattacharya, J. K. Meena, D. C. Biswas, B. N. Joshi, N. Kumar, G. K. Prajapati, Y. K. Gupta, K. Mahata, K. Ramachandran, and S. Pal, Measurement of fragment-mass distributions from fission of ^{214}At following the $^9\text{Be} + ^{205}\text{Tl}$ reaction, *Phys. Rev. C* **102**, 054604 (2020).
- [13] R. Tripathi *et al.*, Fission fragment mass distributions in $^{35}\text{Cl} + ^{144,154}\text{Sm}$ reactions, *Phys. Rev. C* **92**, 024610 (2015).
- [14] J. L. Rodríguez-Sánchez *et al.*, Presaddle and postsaddle dissipative effects in fission using complete kinematics measurements, *Phys. Rev. C* **94**, 061601(R) (2016).
- [15] P. Möller, J. Randrup, and A. J. Sierk, Calculated fission yields of neutron-deficient mercury isotopes, *Phys. Rev. C* **85**, 024306 (2012).
- [16] T. Ichikawa, A. Iwamoto, P. Moller, and A. J. Sierk, The contrasting fission potential-energy structure of actinides and mercury isotopes, *Phys. Rev. C* **86**, 024610 (2012).
- [17] P. Möller and J. Randrup, Calculated fission-fragment yield systematics in the region $74 \leq Z \leq 94$ and $90 \leq N \leq 150$, *Phys. Rev. C* **91**, 044316 (2015).
- [18] T. Ichikawa and P. Möller, The microscopic mechanism behind the fission-barrier asymmetry (II): The rare-earth region $50 < Z < 82$ and $82 < N < 126$, *Phys. Lett. B* **789**, 679 (2019).
- [19] B. Nerlo-Pomorska, K. Pomorski, C. Schmitt, and J. Bartel, Low-energy fission within the Lublin-Strasbourg drop and Yukawa folded model, *Phys. Scr.* **89**, 054031 (2014).
- [20] C. Schmitt, K. Pomorski, B. Nerlo-Pomorska, and J. Bartel, Performance of the Fourier shape parametrization for the fission process, *Phys. Rev. C* **95**, 034612 (2017).
- [21] V. L. Litnevsky, G. I. Kosenko, F. A. Ivanyuk, and V. V. Pashkevich, Description of the two-humped mass distribution of fission fragments of mercury isotopes on the basis of the multidimensional stochastic model, *Phys. At. Nucl.* **77**, 167 (2014).
- [22] A. V. Andreev, G. G. Adamian, and N. V. Antonenko, Mass distributions for induced fission of different Hg isotopes, *Phys. Rev. C* **86**, 044315 (2012).
- [23] A. V. Andreev, G. G. Adamian, N. V. Antonenko, and A. N. Andreyev, Isospin dependence of mass-distribution shape of fission fragments of Hg isotopes, *Phys. Rev. C* **88**, 047604 (2013).
- [24] S. Panebianco, J.-L. Sida, H. Goutte, J.-F. Lemaitre, N. Dubray, and S. Hilaire, Role of deformed shell effects on the mass asymmetry in nuclear fission of mercury isotopes, *Phys. Rev. C* **86**, 064601 (2012).
- [25] M. Veselsky, A. N. Andreyev, S. Antalic, M. Huyse, P. Moller, K. Nishio, A. J. Sierk, P. Van Duppen, and M. Venhart, Fission-barrier heights of neutron-deficient mercury nuclei, *Phys. Rev. C* **86**, 024308 (2012).
- [26] M. Warda, A. Staszczak, and W. Nazarewicz, Fission modes of mercury isotopes, *Phys. Rev. C* **86**, 024601 (2012).
- [27] J. D. McDonnell, W. Nazarewicz, J. A. Sheikh, A. Staszczak, and M. Warda, Excitation energy dependence of fission in the mercury region, *Phys. Rev. C* **90**, 021302(R) (2014).
- [28] G. Scamps and C. Simenel, Effect of shell structure on the fission of sub-lead nuclei, *Phys. Rev. C* **100**, 041602(R) (2019).
- [29] M. Warda and A. Zdeb, Fission fragment mass yield deduced from density distribution in the pre-scission configuration, *Phys. Scr.* **90**, 114003 (2015).
- [30] N. Schunck and L. Robledo, Microscopic theory of nuclear fission: A review, *Rep. Prog. Phys.* **79**, 116301 (2016).
- [31] K.-H. Schmidt and B. Jurado, Review on the progress in nuclear fission—experimental methods and theoretical descriptions, *Rep. Prog. Phys.* **81**, 106301 (2018).
- [32] C. Simenel and A. S. Umar, Heavy-ion collisions and fission dynamics with the time-dependent Hartree-Fock theory and its extensions, *Prog. Part. Nucl. Phys.* **103**, 19 (2018).
- [33] M. Bender *et al.*, Future of nuclear fission theory, *J. Phys. G: Nucl. Part. Phys.* **47**, 113002 (2020).
- [34] M. Verriere and D. Regnier, The time-dependent generator coordinate method in nuclear physics, *Front. Phys.* **8**, 233 (2020).
- [35] N. Schunck and D. Regnier, Theory of nuclear fission, *Prog. Part. Nucl. Phys.* **125**, 103963 (2022).
- [36] Y. Qiang and J. Pei, Energy and pairing dependence of dissipation in real-time fission dynamics, *Phys. Rev. C* **104**, 054604 (2021).
- [37] Y. Qiang, J. C. Pei, and P. D. Stevenson, Fission dynamics of compound nuclei: Pairing versus fluctuations, *Phys. Rev. C* **103**, L031304 (2021).
- [38] M. Pancic, Y. Qiang, J. Pei, and P. Stevenson, Shape evolutions in fission dynamics within time-dependent hartree-fock approach, *Front. Phys.* **8**, 351 (2020).
- [39] A. Bulgac, S. Jin, K. Roche, N. Schunck, and I. Stetcu, Fission dynamics of ^{240}Pu from saddle to scission and beyond, *Phys. Rev. C* **100**, 034615 (2019).
- [40] P. M. Goddard, P. D. Stevenson, and A. Rios, Fission dynamics within time-dependent Hartree-Fock: Deformation-induced fission, *Phys. Rev. C* **92**, 054610 (2015).
- [41] P. Goddard, P. D. Stevenson, and A. Rios, Fission dynamics within time-dependent Hartree-Fock. II. Boost-induced fission, *Phys. Rev. C* **93**, 014620 (2016).
- [42] G. Scamps, C. Simenel, and D. Lacroix, Superfluid dynamics of ^{258}Fm fission, *Phys. Rev. C* **92**, 011602(R) (2015).
- [43] A. S. Umar, V. E. Oberacker, and C. Simenel, Shape evolution and collective dynamics of quasifission in the time-dependent Hartree-Fock approach, *Phys. Rev. C* **92**, 024621 (2015).
- [44] H. Goutte, P. Casoli, and J. F. Berger, Mass and kinetic energy distributions of fission fragments using the time dependent generator coordinate method, *Nucl. Phys. A* **734**, 217 (2004).
- [45] D. Regnier, N. Dubray, N. Schunck, and M. Verrière, Fission fragment charge and mass distributions in $^{239}\text{Pu}(n, f)$ in the adiabatic nuclear energy density functional theory, *Phys. Rev. C* **93**, 054611 (2016).
- [46] D. Regnier, M. Verrière, N. Dubray, and N. Schunck, FELIX-1.0: A finite element solver for the time dependent generator coordinate method with the Gaussian overlap approximation, *Comput. Phys. Commun.* **200**, 350 (2016).
- [47] A. Zdeb, A. Dobrowolski, and M. Warda, Fission dynamics of ^{252}Cf , *Phys. Rev. C* **95**, 054608 (2017).
- [48] D. Regnier, N. Dubray, and N. Schunck, From asymmetric to symmetric fission in the fermium isotopes within the time-dependent generator-coordinate-method formalism, *Phys. Rev. C* **99**, 024611 (2019).
- [49] W. Younes and D. Gogny, Fragment Yields Calculated in a Time-Dependent Microscopic Theory of Fission, Tech. Rep. No. LLNL-TR-586678, Lawrence Livermore National Security, Livermore, 2012.
- [50] D. Regnier, N. Dubray, N. Schunck, and M. Verrière, Microscopic description of fission dynamics: Toward a 3D

- computation of the time dependent GCM equation, *EPJ Web Conf.* **146**, 04043 (2017).
- [51] H. Tao, J. Zhao, Z. P. Li, T. Nikšić, and D. Vretenar, Microscopic study of induced fission dynamics of ^{226}Th with covariant energy density functionals, *Phys. Rev. C* **96**, 024319 (2017).
- [52] J. Zhao, J. Xiang, Z.-P. Li, T. Nikšić, D. Vretenar, and S.-G. Zhou, Time-dependent generator coordinate method study of mass-asymmetric fission of actinides, *Phys. Rev. C* **99**, 054613 (2019).
- [53] J. Zhao, T. Nikšić, D. Vretenar, and S.-G. Zhou, Microscopic self-consistent description of induced fission dynamics: Finite temperature effects, *Phys. Rev. C* **99**, 014618 (2019).
- [54] J. Zhao, T. Nikšić, D. Vretenar, and S.-G. Zhou, Time-dependent generator coordinate method study of fission: Mass parameters, *Phys. Rev. C* **101**, 064605 (2020).
- [55] J. Zhao, T. Nikšić, and D. Vretenar, Microscopic self-consistent description of induced fission: Dynamical pairing degree of freedom, *Phys. Rev. C* **104**, 044612 (2021).
- [56] J. Zhao, T. Nišić, and D. Vretenar, Time-dependent generator coordinate method study of fission: Dissipation effects, *Phys. Rev. C* **105**, 054604 (2022).
- [57] A. Bulgac, P. Magierski, K. J. Roche, and I. Stetcu, Induced Fission of ^{240}Pu within a Real-Time Microscopic Framework, *Phys. Rev. Lett.* **116**, 122504 (2016).
- [58] Y. Tanimura, D. Lacroix, and S. Ayik, Microscopic Phase-Space Exploration Modeling of ^{258}Fm Spontaneous Fission, *Phys. Rev. Lett.* **118**, 152501 (2017).
- [59] A. Bulgac, S. Jin, and I. Stetcu, Unitary evolution with fluctuations and dissipation, *Phys. Rev. C* **100**, 014615 (2019).
- [60] R. Han, M. Warda, A. Zdeb, and L. M. Robledo, Scission configuration in self-consistent calculations with neck constraints, *Phys. Rev. C* **104**, 064602 (2021).
- [61] D. Regnier, N. Dubray, M. Verrière, and N. Schunck, FELIX-2.0: New version of the finite element solver for the time dependent generator coordinate method with the Gaussian overlap approximation, *Comput. Phys. Commun.* **225**, 180 (2018).
- [62] W. Younes and D. Gogny, Microscopic calculation of ^{240}Pu scission with a finite-range effective force, *Phys. Rev. C* **80**, 054313 (2009).
- [63] P. W. Zhao, Z. P. Li, J. M. Yao, and J. Meng, New parametrization for the nuclear covariant energy density functional with point-coupling interaction, *Phys. Rev. C* **82**, 054319 (2010).